Ligand tuneable, red-emitting iridium(III) complexes for efficient triplet-triplet annihilation upconversion performance

Kaitlin A. Phillips,[a] Thomas M. Stonelake, [a] Kepeng Chen, [b] Yuqi Hou, [b] Jianzhang Zhao, [b] Simon J. Coles, [c] Peter N. Horton, [c] Shannon J. Keane, [a] Emily C. Stokes, [a] Ian A. Fallis, [a] Andrew J. Hallett,[d] Sean P. O'Kell,[d] Joseph M. Beames,* [a] and Simon J.A. Pope*[a]

[a] K.A. Phillips, T.M. Stonelake, S. J. Keane, Dr E.C. Stokes, Dr I.A. Fallis, Dr J.M. Beames, Prof. S.J.A. Pope
School of Chemistry, Main Building
Cardiff University
Cardiff, CF10 3AT (UK)
E-mail: beamesj@cardiff.ac.uk; popesj@cardiff.ac.uk
[b] K. Chen, Y. Hou, Prof. J. Zhao
State Key Laboratory of Fine Chemicals
Dalian University of Technology
Dalian 116024 (P.R. China)
[c] Prof. S.J. Coles, Dr P.N. Horton
UK National Crystallographic Service, Chemistry,
University of Southampton, Highfield, Southampton, SO17 1BJ (UK)
[d] Dr A.J. Hallett, Dr S. P. O'Kell
STG Aerospace, Brecon House,
Cwmbran, NP44 3AB (UK)

Abstract: A series of substituted 2-phenylquinoxaline ligands have been explored to finely tune the visible emission properties of a corresponding set of cationic, cyclometalated iridium(III) complexes. The electronic and redox properties of the complexes were investigated using experimental (including time-resolved luminescence and transient absorption spectroscopy) and theoretical methods. The complexes display absorption and phosphorescent emission in the visible region attributed to MLCT transitions. The different substitution patterns of the ligands induce variations in these parameters. TD-DFT studies support these assignments and show that there is likely to be a strong spin-forbidden contribution to the visible absorption bands at 500-600 nm. Calculation also reliably predict the magnitude and trends in triplet emitting wavelengths for the series of complexes. The complexes were assessed as potential sensitizers in triplet-triplet annihilation upconversion experiments using 9,10-diphenylanthracene as the acceptor, with the methylated variants performing especially well with impressive upconversion quantum yields up to 39.3 %.

Introduction

Photoactive metal coordination compounds continue to find broadening application in several disciplines such as electroluminescence, photovoltaics, photocatalysis, and bioimaging. In particular, organometallic Ir(III) complexes are extremely attractive as a wide range of ligand architectures exist and can be developed to allow tuning of the excited state properties of such complexes.[1] A more recent development in their potential application is in the field of triplet-triplet annihilation (TTA) upconversion[2] where such species, through a limited number of studies,[3] appear to be well suited to use as sensitizers which stimulate fluorescence from an appropriate annihilator acceptor molecule. TTA upconversion is of great interest due to the benefits that such processes can provide to the disciplines outlined earlier. A small number of reports have described the use of Ir(III) complexes for TTA upconversion[4] with the best performing to date being pyrene-conjugated species of the type $[Ir(ppy)_2(L)]PF_6$ which demonstrated highly efficient upconversion quantum yields of up to 31.6 % (the highest value yet reported).[5] Typically, the sensitizer should possess good molar absorption at the wavelength of excitation and a long triplet lifetime.[6]

Our own work into luminescent Ir(III) complexes has included the development of low energy emitting species that luminesce in the red part of the visible spectrum. The requisite cyclometalating ligands are based upon core ligand structures of 2-phenylquinoline[7] or 2-phenylquinoxaline[8] and these can provide interesting species with related pyrene derivatives also showing capability as potent photooxidation sensitizers.[9] Other studies have reported extending the emission wavelengths of Ir(III) complexes into the NIR region.[10]

In the current work, we have focused upon the development of poly-substituted quinoxaline ligands to tune the emission of a new series of cationic cyclometalated Ir(III) complexes. The ability to finely tune the excited state character and energy of the complex is essential when considering applications such as TTA upconversion. The structural and spectroscopic characterisation of these complexes together with detailed theoretical analysis has provided further insight into the species and their application to TTA upconversion. We now report a world-leading TTA upconversion efficiency of 39.3% from one of the iridium complexes within our series of newly synthesized phosphors.

Results and Discussion

All ligands (Scheme 1) were synthesised by heating the required phenyldiamine with benzil or 1-phenyl-1,2-propanedione in ethanol in the presence of acetic acid. The ligands were reacted with iridium trichloride to generate the chloro-bridged dimetallic $[Ir(L)_2\text{-}\mu\text{-}Cl]_2$ species,[11] which were subsequently reacted with 2,2'-bipyridine in 2-ethoxyethanol at 120° to yield the corresponding monometallic species $[Ir(L)_2(bpy)]PF_6$ following precipitation with NH_4PF_6 (sat. aq.). These reaction conditions are known to favour the *cis*-C,C and *trans*-N,N coordination mode for the cyclometalating ligand at Ir(III) and have been supported by structural data.[12] Other studies have shown that the mutual *cis*-C,C and *cis*-N,N arrangement of certain cyclometalating ligands can be achieved using different reaction conditions.[13] If required, further purification was achieved using column chromatography (silica) by eluting a major red band with DCM/MeOH (95/5). All complexes (Scheme 1) were isolated as reddish brown air-stable solids. **L1** has been previously reported, but all characterisation data are included in the Experimental section for convenience and comparison.[14]

The complexes were characterized using multinuclear NMR, IR, UV-vis., transient absorption and luminescence spectroscopies, as well as HRMS, cyclic voltammetry and X-ray diffraction. ^{1}H NMR spectra provided clear evidence for the formation of the complexes with characteristic shifts in the various resonances associated with the quinoxaline ligands. In particular, the proton adjacent to the cyclometalated carbon was shifted upfield in all cases indicative of the shielding effect of coordination to iridium(III). For **$[Ir(L1)_2(bpy)]PF_6$**, **$[Ir(L2)_2(bpy)]PF_6$** and **$[Ir(L3)_2(bpy)]PF_6$** the methyl resonance(s) were shifted away from the corresponding free ligand values. ^{19}F{^{1}H} NMR spectroscopy was used to analyse **$[Ir(L4)_2(bpy)]PF_6$** and **$[Ir(L7)_2(bpy)]PF_6$** and revealed (Table 1) observable differences in the ^{19}F resonances in the spectra. Firstly, for the ligand-based fluorines, typical shifts were observed around -131 ppm; these were subtly shifted upon coordination when compared to the free ligands. A loss of chemical equivalence in the **L7** fluorines was anticipated upon cyclometalation via the expected coordination mode, and this manifested in a $^3J_{FF}$ coupling of around 22 Hz.[15] Both complexes showed an additional chemical shift *ca*. -73 ppm which is assigned to the non-coordinating hexafluorophosphate. Examples of obtained NMR spectra are shown in the ESI

Figures S1-S5. The observations from the NMR data are consistent with the presence of a single isomer of complex in each case.

<Scheme 1>

HRMS data were obtained for each of the complexes confirming the proposed formulations and showing the expected isotopic distributions in each case; the dichloro species, in particular, produced distinct spectra. Supporting IR data principally indicated the presence of the coordinated ligands in each case and the hexafluorophosphate counter anion at *ca*. 840 cm^{-1}.

Table 1. $^{19}F\{^{1}H\}$ NMR chemical shift and coupling constant values for the fluorinated ligands and complexes.

Compound[a]	Ligand δ ($^{3}J_{FF}$) / ppm	PF_6^- δ ($^{1}J_{FP}$) / ppm
L4	-130.4 (d, 21 Hz), -131.2 (d, 21 Hz)	
$[Ir(L4)_2(bpy)]PF_6$	-131.7 (d, 22 Hz), -133.7(d, 22 Hz)	-72.6 (d, 712 Hz)
L7	-129.9 (s)	
$[Ir(L7)_2(bpy)]PF_6$	-130.3 (d, 22 Hz), -132.7 (d, 22 Hz)	-72.6 (d, 700 Hz)

X-ray Crystallography

X-ray quality single crystals were obtained for two of the methylated species **$[Ir(L2)_2(bpy)]PF_6$**, **$[Ir(L5)_2(bpy)]PF_6$** and the difluoro variant **$[Ir(L7)_2(bpy)]PF_6$** *via* a vapour diffusion methodology (diethyl ether into acetonitrile solutions). Data collection parameters are reported in ESI, Table S1, whilst key bond length/angle data are shown in ESI, Tables S2 and S3. Each complex adopts a distorted octahedral geometry at Ir(III) with substituted quinoxaline ligands chelating in a N^C fashion (Figure 1). The obtained structures confirm the expected *cis*-C,C and *trans*-N,N arrangements of the cyclometalating ligands that are retained irrespective of the quinoxaline ligand substitution. The observation support previous assertions about the stronger trans influence of the phenyl group over nitrogen heterocycle donors.[16] Bond

lengths to Ir(III) lie in the typical range expected for such species. Additional packing diagrams are shown in the ESI showing that intermolecular pi-pi contacts are present between phenyl rings on the quinoxaline ligands of neighbouring complexes.

Figure 2 shows a comparison of the experimental crystal structure of **[Ir(L5)$_2$(bpy)]PF$_6$** with the computationally optimized structure. The figure demonstrates that the computational method chosen serves to adequately reproduce the crystal structure (RMSD < 0.5 Å) with the majority of the discrepancy being introduced by the position of the methyl substituent groups, which likely derives from a combination of errors in crystallography and DFT. This is to be expected given the low frequency vibrational motions associated with both the flexing and torsional motions of these methyl groups. Some discrepancy is observed with the bipyridine position, such that the computed geometry is closer to C_2 symmetry.

<Figure 1>

<Figure 2>

Electronic properties of the complexes

The UV-vis. absorption properties of the complexes were determined using chloroform solutions. Between 260-400 nm the complexes show a composite of high probability transitions that overlap with one another. The bands are generally ascribed to the different ligand-centred transitions relating to the coordinated quinoxaline and bipyridine ligands. They are likely to comprise of various $\pi \rightarrow \pi^*$ transitions with the possibility of weaker $n \rightarrow \pi^*$ arising from the heterocyclic quinoxaline core. The spectra show a strong feature at 400-450 nm, and a weaker, broad, lower energy band peaking at 474-498 nm (the associated molar absorption coefficients are *ca*. 5×10^3 $M^{-1}cm^{-1}$); transitions which are likely to possess some MLCT character. The positioning of these bands are clearly dependent upon the substitution of the cyclometalated quinoxaline ligand: the halogenated complexes show the longest wavelength values whilst the methylated analogues are, in contrast, hypsochomically shifted (Figure 3). All visible region features showed a weaker lower energy shoulder that extended to *ca*. 600 nm in these complexes. For related iridium(III) complexes this observation has been previously attributed to the transition to the spin forbidden

^{3}MLCT state. Further discussion of the nature of these electronic transitions is provided below.

The electrochemical characteristics of the complexes were studied in de-oxygenated dichloromethane. The cyclic voltammograms were measured using a platinum disc electrode (scan rate u = 200 mV s^{-1}, 1 × 10^{-3} M solutions, 0.1 M $[NBu_4][PF_6]$ as a supporting electrolyte). Each complex showed an irreversible oxidation process between +1.4 and +1.6 V, which is assigned to a $Ir^{3+}/^{4+}$ process. The methyl-substituted complexes of **L1**, **L2** and **L5** possessed the lowest E_{ox} values consistent with the anticipated electron donating ability of the quinoxaline ligands. An irreversible signal around -0.9 V was also observed and is assigned to a ligand-centred reduction.

<Figure 3>

Density functional theory

Figure S8 (ESI) illustrates the Kohn-Sham frontier orbitals for complex **$[Ir(L1)_2(bpy)]PF_6$** in chloroform. The orbitals are shown at the minimum energy geometry on the S_0 surface. The orbitals illustrate that the occupied molecular orbitals (MO) have strong Ir(5*d*) character, whereas the unoccupied orbitals are more ligand centred. This is confirmed through MO decomposition analysis (see Table S4, ESI, GaussSum Package[17]): the highest occupied molecular orbital (HOMO) has equal MO contributions from the metal (33%) and the two identical quinoxaline ligands (33% and 33%), with a negligible contribution from the bipyridine (1%). In contrast, the lowest unoccupied molecular orbital (LUMO) is predominantly centred on the quinoxalines (48% and 47%). All complexes exhibit similar orbital contributions, however **$[Ir(L5\text{-}L7)_2(bpy)]PF_6$** have slightly reduced metal contributions to the HOMO, between 28% and 30%. The contributions from the quinoxaline ligands are necessarily near degenerate given the symmetric nature of the system. These orbital descriptions afford further analysis of the excited states of this system. TD-DFT calculations suggest the character of all the singlet excited states (that lie in a region of interest, 250 nm < λ < 750 nm) are reasonably mixed, however most of the occupied MOs have sizeable Ir(5*d*) contributions, the HOMO-1 being the notable exception, and all the unoccupied orbitals ligand centred, with

< 5% metal contributions, therefore each state will possess a significant degree of ^{1}MLCT character. The longest wavelength singlet excitation is predicted to be at λ = 405 nm, and does not account for the broad structureless feature observed in the absorption spectrum with $\lambda_{max} \approx$ 475 nm, typically attributed to the formally spin forbidden $T_1 \leftarrow S_0$, which may become weakly allowed due to spin-orbit effects. This is in reasonable agreement with the comparison between the energy of the T_1 state at the geometry of the S_0 ground state minimum, which corresponds to a predicted ^{3}MLCT band at λ = 514 nm. These transitions all compare qualitatively favourably with the observed UV-vis. spectrum of **[Ir(L1)$_2$(bpy)]PF$_6$**, as shown in Figure 4.

Optimization of triplet **[Ir(L1)$_2$(bpy)]PF$_6$,** affords an examination of the spin-forbidden emission bands of the complex. This procedure leads to a significant underestimation of the energy of the spin forbidden band: the computed vertical transition occurs at 719 nm, with the experimental observation of this band ($\lambda_{max} \approx$ 630 nm). This observation could be attributed to the evolution of the system from an initially prepared singlet photoexcited state into a higher lying triplet state from which emission occurs (TD-DFT calculations suggest, for example, that there are three additional triplet states within 0.3 eV of T_1 within the Franck-Condon region). However, Kasha's rule would suggest that ^{3}MLCT emission occurs after photoexcitation at the S_0 minimum energy geometry; whereupon it is assumed the ISC, IC and IVR processes occur rapidly in the excited states, such that phosphorescence occurs from the relaxed T_1 geometry. The T_1 geometry relaxation primarily involves additional buckling of a single quinoxaline ligand, and a more subtle change in the bipyridine.

Despite the relatively subtle changes in the triplet state geometry, these complexes exhibit a range of low frequency vibrational modes, leading to a very broad Franck-Condon envelope for these electronic transitions. A cursory investigation of the emission band profile of **[Ir(L1)$_2$(bpy)]PF$_6$** at 298 K, utilizing the Franck-Condon procedures in the Gaussian 09 suite,[18] exclusive of Herzberg-Teller interactions, shows that indeed the emission profile will be broad, and spans the wavelength region over which phosphorescence is observed, leading to the conclusion that emission is indeed observed from T_1. Such a methodology is quantitatively problematic for system of this size and with such a number of low frequency vibrational modes, but provides a qualitative depiction of the complex emission. As shown in Figure S9 (ESI), this simulation provides good agreement with the experimentally recorded emission band,

reasonably well reproducing both the λ_{max} value, and the band contour. From the simulation it can be extracted that the band profile is predominantly formed by a progression in mixed C-C stretch/C-C-C bend modes localized on the quinoxaline ligands (~1400 cm^{-1}). This is in good agreement with the electron density change induced by the ^{3}MLCT emission. These vibronic features are broadened by multiple combinations of low frequency modes. In addition, the calculations illustrate the adiabatic transition values are a more appropriate model of emission band positions (Table 2). These data illustrate that the dichloro –complexes exhibit substantial bathochromic shifts, in good agreement with experiment.

<Figure 4>

A more complete investigation of the vibronic band shapes and Franck-Condon effects was performed on the $S_1/T_1 \leftarrow S_0$ computed spectral features for **[Ir(L1)$_2$(bpy)]PF$_6$.** Photoabsorption cross sections were computed by sampling over the ground state (S_0) geometries accessible at room temperature using a nuclear ensemble method, implemented in the Newton-X computational suite.[19,20] In this case, 2000 geometries (N_s) were sampled from an uncoupled harmonic oscillator Wigner distribution such that they describe a ground state (S_0) quantum distribution, with excitation energies (E_{0n}) and oscillator strengths (f_{0n}) for the first ten singlet states (N_n) and first 5 triplet states, computed at each geometry ($\boldsymbol{R_k}$), and then summed (with a δ = 0.2 eV Lorentzian convolution [red]) to construct the photoabsorption cross section ($\sigma(E)$).

This methodology can be used to provide band shapes and relative cross sections for electronic transitions, but unlike the Franck-Condon method described above, does not reproduce vibronic progressions. It is worth noting the refractive index for all calculations is assumed to be 1. This assessment of band shapes is extremely computationally costly and has only been applied to **[Ir(L1)$_2$(bpy)]PF$_6$**, in order to demonstrate the accuracy of the band assignments.

$$\sigma(E) = \frac{\pi e^2 \gamma}{2mc\varepsilon_0} \sum_{l\neq 0}^{N_s} \frac{1}{N_n^l} \sum_{k}^{N_n^l} f_{0l}(\boldsymbol{R}_k)\, g(E - E_{0n}(\boldsymbol{R}_l), \delta)$$

Table 2. Computed spectral properties for all complexes alongside experimentally observed band positions in parentheses. The experimental spin allowed absorption band positions are taken from the band onsets, whereas the spin forbidden parameters are λ_{max} values for the respective bands. Shaded rows highlight **L5**-**L7** phenyl substituted analogues of **L2**-**L4**. Both vertical and adiabatic emission energies are reported, the latter in italics.

Compound[a]	$S_1 \leftarrow S_0$ (nm) [a]	$T_1 \leftarrow S_0$ (nm) [b]	$T_1 \rightarrow S_0$ (nm) [b]
$[Ir(\mathbf{L1})_2(bpy)]PF_6$	405 (372)	541 (477)	691, *607* (627)
$[Ir(\mathbf{L2})_2(bpy)]PF_6$	402 (402)	533 (474)	698, *605* (617)
$[Ir(\mathbf{L3})_2(bpy)]PF_6$	419 (406)	565 (500)	708, *630* (634)
$[Ir(\mathbf{L4})_2(bpy)]PF_6$	409 (394)	552 (480)	692, *612* (624)
$[Ir(\mathbf{L5})_2(bpy)]PF_6$	406 (417)	540 (479)	723, *618* (624)
$[Ir(\mathbf{L6})_2(bpy)]PF_6$	423 (428)	572 (501)	730, *642* (645)
$[Ir(\mathbf{L7})_2(bpy)]PF_6$	414 (418)	555 (483)	716, *626* (632)

[a] Recorded in chloroform. [b] In chloroform, λ_{ex} = 355 nm

Given the remarkable agreement between the absorption spectrum of **$[Ir(L1)_2(bpy)]PF_6$** and the computational spectral simulation, the relative band positions of all the complexes have been computed, and are displayed in Table 2.

<Figure 5>

Table 3. Emission data of the complexes recorded in chloroform. Shaded rows highlight **L5**-**L7** phenyl substituted analogues of **L2**-**L4**.

Compound	λ_{em} / nm [a,b]	τ / μs [a,c]	Φ_{em} [a]	k_r / s^{-1} $\times 10^5$	k_{nr} / s^{-1} $\times 10^6$
$[Ir(L1)_2(bpy)]PF_6$	627	0.46	5.7	1.2	2.1
$[Ir(L2)_2(bpy)]PF_6$	617	0.45	5.1	1.1	2.1
$[Ir(L3)_2(bpy)]PF_6$	634	0.34	1.8	0.32	2.9
$[Ir(L4)_2(bpy)]PF_6$	624	0.40	6.0	1.5	2.4
$[Ir(L5)_2(bpy)]PF_6$	624	0.44	6.6	1.5	2.1
$[Ir(L6)_2(bpy)]PF_6$	645	0.31	6.4	2.1	3.0
$[Ir(L7)_2(bpy)]PF_6$	632	0.54	7.8	1.4	1.1

[a] In chloroform; [b] In chloroform, λ_{ex} = 480 nm; [c] Luminescence lifetime in chloroform, λ_{ex} = 459 nm; [d] Quantum yield with $[Ru(bpy)_3][PF_6]_2$ as standard (Φ_Δ = 0.018 in acetonitrile).[21]

The complexes showed emission properties in the visible region (Figure 5). Steady state measurements in both chloroform (Table 3) and toluene (Table 4) confirmed that the complexes emit with a broad feature at 550-750 nm. The coordinated quinoxaline ligands modulate the emission energy of the complexes with the trimethylated species

[Ir(L2)$_2$(bpy)]PF$_6$ revealing the highest energy emission, and the dichloro- analogues displaying the most bathochromic shift within the series. The shift to longer wavelength upon chlorination is a result of changing electronic character of the system, demonstrated clearly by the reproducibility of this trend in the $T_1 \leftarrow S_0$ TD-DFT calculations (Table 2), and equally borne out by the shift in $S_1 \leftarrow S_0$ band onsets. However, the cause of the reduced emission lifetimes for the chlorinated species cannot be deconvoluted from a mixture of electronic and relativistic effects, and indeed an increase in ISC rates (supported by increased k_{nr} contributions) may be anticipated for the dichloro- species.

In order to validate the hypothesis that chlorine substitution of the quinoxaline ligands leads to an increase S_0/T_1 spin orbit couplings (SOC), SOC elements have been computed from LR-TDDFT calculations at the T_1 minimum energy geometries for **[Ir(L1)$_2$(bpy)]PF$_6$** and **[Ir(L6)$_2$(bpy)]PF$_6$**. Values are generated utilising a Breit-Pauli SO operator based approach, recently implemented in the PySOC computational suite. These calculations suggest that the SOC elements, $< S_0 \mid H_{SO} \mid T_1 >$, evaluated as the root of the squared sum of the m_s sublevels, is larger (5%, 149 cm^{-1} vs 142 cm^{-1}) for the chlorinated **[Ir(L6)$_2$(bpy)]PF$_6$** than for **[Ir(L1)$_2$(bpy)]PF$_6$**. This change is characteristic of a reduced T_1 lifetime for the chloro-substituted systems, and along with the electronic shift in the potential energy surfaces, serves to explain the photophysics of the molecule.

Experimental time-resolved luminescence lifetime measurements showed monoexponential decay character in each case, consistent with a single emitting state. These observed lifetimes confirmed the phosphorescent nature of the emission for all complexes, and corresponding degassed measurements indicated sensitivity to quenching via $^3O_2$, with lifetimes typically extending into the microsecond domain. Thus, all the photophysical data are consistent with an emitting state that possesses significant ^{3}MLCT character.

Transient absorption spectroscopy

Transient absorption (TA) spectroscopy was carried out on each of the complexes using chloroform solutions. All the spectra are similar in appearance, and once again complex **[Ir(L1)$_2$(bpy)]PF$_6$** is chosen as an example for further discussion. The spectrum shown in Figure 6 is illustrative of TA spectra for all of the complexes described herein. From short to long wavelength, the spectrum shows a ground state

bleach (negative ΔOD) at λ = 355 nm, two features corresponding to putative triplet-triplet absorptions in the visible (λ_{max} ≈ 430 nm and 560 nm, respectively) and finally a long wavelength emission attributed to the spin-forbidden $T_1 \rightarrow S_0$ radiative transition. The two triplet absorption bands are consistent with TD-DFT calculations which suggests that there are a set of strong $T_n \leftarrow T_1$ absorption bands at λ < 600 nm. The longest wavelength, negative-going peak is assigned based on the similarity between the TA feature (black) and the emission profile (red).

<Figure 6>

Each feature, including the ground state bleach and recovery, and the phosphorescence, exhibit similar TA lifetimes (right of figure 6), suggesting that each peak relates to the same photoexcitation, intersystem crossing (ISC) process and deactivation. This is attributed to the formation of the lowest triplet state, via prompt S_1/T_1 ISC and compare relatively well to the observed lifetime from time-resolved emission measurements.[22] Figure 7 displays a comparison of transient absorption spectra for the complexes **[Ir(L1)$_2$(bpy)]PF$_6$**, **[Ir(L5)$_2$(bpy)]PF$_6$** and **[Ir(L6)$_2$(bpy)]PF$_6$**. Each spectrum shows qualitatively similar features, with the exception of the ground state bleach <450 nm, which appears to be a clear doublet in the case of **[Ir(L5)$_2$(bpy)]PF$_6$** and **[Ir(L6)$_2$(bpy)]PF$_6$**, but does not show the same spectral shape for **[Ir(L1)$_2$(bpy)]PF$_6$**. For each of the complexes the temporal evolution (Fig. 8) of the four transient absorption features described in Figure 7 have been analysed in an analogous fashion and are shown in Table S5 (ESI), alongside the spin-forbidden emission lifetimes, duplicated from Table 2.

<Figure 7>

<Figure 8>

TTA upconversion measurements

TTA upconversion luminescence experiments were conducted in degassed toluene using the complexes as the donor component and 9,10-diphenylanthracene (DPA) as the acceptor. The spectra in Figure 9 show the recorded emission spectra in degassed

toluene for these upconversion experiments. In each case the graphs contain superimposed emission profiles for the native complex and the complex/DPA mixture following excitation at 510 nm. The DPA triplet excited state is at 700 nm (1.77 eV) and therefore lies below the triplet emitting level of all of the complexes in the series. Direct irradiation of DPA using 510 nm does not produce any emission. In contrast, for the majority of the complex/DPA mixtures, fluorescence from DPA was observed at 400-500 nm which is therefore indicative of an upconversion process. This was most pronounced for **[Ir(L1)$_2$(bpy)]PF$_6$**, **[Ir(L2)$_2$(bpy)]PF$_6$** and **[Ir(L5)$_2$(bpy)]PF$_6$** which display a concomitant quenching of the ^{3}MLCT emission band at 600-700 nm.

<Figure 9>

These observations were quantitatively supported by the measured quantum yields for upconversion (Table 4) which showed significant variation across the series of complexes. Interestingly, the methylated variants performed best, amongst which **[Ir(L1)$_2$(bpy)]PF$_6$** and **[Ir(L2)$_2$(bpy)]PF$_6$** displayed remarkable efficiencies of 26% and 39%, respectively. The latter is the highest recorded value for TTA upconversion with a triplet sensitiser.

<Figure 10>

In comparison, the upconversion performance was contrastingly low (≤ 1%) for both dichloro-species **[Ir(L3)$_2$(bpy)]PF$_6$** and **[Ir(L6)$_2$(bpy)]PF$_6$**. Previous reports in the literature have highlighted high molar absorption coefficients in the visible region and long triplet excited state lifetimes as advantageous attributes for triplet sensitizers.[23] It is notable that these complexes possess modest triplet state lifetimes and molar absorption values around 5000 $M^{-1}cm^{-1}$ in the visible region at *ca*. 500 nm. The luminescence data in toluene revealed a larger variation in emission properties with the methylated variants displaying the highest emission energies and the longest triplet state lifetimes. The poorly performing dichloro- derivatives show the longest wavelength emission maxima and shortest triplet lifetimes. The difluoro-substituted

complexes perform slightly better than the dichloro analogues, probably reflecting the longer triplet lifetime values.

Table 4. Emission and upconversion data of the complexes recorded in toluene. Shaded rows highlight **L5**-**L7** phenyl substituted analogues of **L2**-**L4**.

Compound	λ_{em} / nm [a,b]	τ_{obs} / μs [b]	τ_{obs} / μs [c]	Φ_{UC} / % [d]
$[Ir(L1)_2(bpy)]PF_6$	618	0.41	2.2	25.9
$[Ir(L2)_2(bpy)]PF_6$	609	0.38	2.3	39.3
$[Ir(L3)_2(bpy)]PF_6$	656	0.38	0.8	0.1
$[Ir(L4)_2(bpy)]PF_6$	638	0.39	1.8	2.0
$[Ir(L5)_2(bpy)]PF_6$	617	0.37	2.0	9.6
$[Ir(L6)_2(bpy)]PF_6$	660	0.35	1.8	1.0
$[Ir(L7)_2(bpy)]PF_6$	646	0.38	1.3	4.0

[a] In toluene (1.0×10^{-5} M); [b] Luminescence lifetime in air, λ_{ex} = 510 nm; [c] Luminescence lifetime in deaerated toluene, λ_{ex} = 510 nm; [d] TTA upconversion quantum yield (Φ_{UC}) with diiodo–Bodipy as standard (Φ_F = 0.027 in acetonitrile).

The visual representation of the upconversion was photographically recorded for the best performing methylated complexes and is shown in Figure 10. The variation in visual appearance can be plotted using CIE coordinates (Fig. 11) and conveniently demonstrates the tuneability of the system. The observed red emission of the parent triplet sensitizers is dramatically shifted upon addition of DPA to give new CIE coordinates.

<Figure 11>

Conclusions

The use of substituted quinoxaline ligands as cyclometalating units for iridium(III) has proven to be a highly efficient route towards the development of high performance sensitizers for triplet-triplet annihilation upconversion. Methylation of the coordinated quinoxaline heterocycle increases the energy and the lifetime of the triplet state emission and thus enhances performance. In contrast, whilst chloro-substitution bathochromically shifts the absorption and emission profiles, the dramatic reduction in triplet state lifetime for the complex of **L3** proves unfavourable with respect to TTA upconversion efficiency. We attribute this, with supporting calculations, to the

enhancement in ISC assisted by the chlorine substituents that leads to more rapid non-radiative deactivation of the ^{3}MLCT state.

Experimental Section

X-ray crystallography

Suitable crystals for **[Ir(L2)$_2$(bpy)]PF$_6$**, **[Ir(L5)$_2$(bpy)]PF$_6$** and **[Ir(L7)$_2$(bpy)]PF$_6$** were obtained and mounted on a MITIGEN holder in perfluoroether oil on a Rigaku FRE+ equipped with either VHF Varimax confocal mirrors and an AFC12 goniometer and HyPix 6000 detector diffractometer (**[Ir(L5)$_2$(bpy)]PF$_6$**) or HF Varimax confocal mirrors and an AFC12 goniometer and HG Saturn 724+ detector diffractometer (**[Ir(L2)$_2$(bpy)]PF$_6$** and **[Ir(L7)$_2$(bpy)]PF$_6$**).[24] The crystal was kept at T = 100(2) K during data collection. Using Olex2[25] the structure was solved with the ShelXT [26] structure solution program, using the Intrinsic Phasing solution method. The model was refined with version 2014/7 of ShelXL[27] using Least Squares minimisation. All non-H atoms were refined anisotropically and difference Fourier syntheses were employed in positioning idealized hydrogen atoms and were allowed to ride on their parent C-atoms. For sample **[Ir(L5)$_2$(bpy)]PF$_6$** there was highly disordered solvent (assumed to be either MeCN, ether or a mixture) that could not be suitably modelled. As such solvent masking within Olex2 was applied. Due to the quality of the crystals for sample **[Ir(L7)$_2$(bpy)]PF$_6$** a significant number of restraints (RIGU, SADI, BUMP) were required.

Computational methods

Electronic structure calculations were all performed using density fitted-density functional theory within the Gaussian 09 computational chemistry suite.[vi] All calculations were performed using the Stuttgart-Dresden (SDD) effective core potential and basis set in the treatment of the iridium, in combination with a 6-31G* basis set for all other light atoms. Full geometry optimizations were performed for the cationic complexes utilizing the self-consistent reaction field model (SCRF) which treats the solvent implicitly as a dielectric continuum. In all cases the solvent chosen was chloroform, consistent with that utilized in the both final synthesis and in the

majority of the spectroscopic measurements. Chloroform is characterized by an electrical permittivity of ε = 4.7113 within the calculations. This computational method models the solvent as surrounding a cavity in which the solute resides, and this cavity is characterized using an integral equation formalism for the polarizable continuum model (IEFPCM). This model represents the system in equilibrium during, for example, an optimization routine: in all excited state calculations a non-equilibrium solvent model is used.

All geometry optimizations were performed using an ultrafine grid and very tight convergence criteria, and the minima were confirmed as stationary points through the computation of harmonic vibrational frequencies, each of which showed no imaginary components. These stationary points were used in single point TD-DFT calculations to compute vertical excitation energies. All TD-DFT calculations were undertaken using a linear response approach. All TD-DFT calculations were also performed with a long range corrected hybrid functional (CAM-B3LYP).

Phosphorescence and spin-forbidden absorption bands were investigated using unrestricted density functional theory to compute parameters associated with the first triplet state (T_1), using an identical methodology as for the singlet states. Decomposition of the molecular orbital character was performed using the GaussSum software package. Crystal structure overlays with optimised computational structures has been performed using the Chimera software package, which has also been used to calculate root mean squared deviation (RMSD) values for these comparative structures.[28]

Transient absorption measurements

Transient absorption measurements were carried out using an Edinburgh Instruments LP920 spectrometer. All spectra were collected using a pump wavelength of 355 nm (third harmonic of a Continuum Surelite II Nd:YAG laser system). The probe light for these measurements was a Xenon lamp, affording spectral generation between $300 < \lambda < 800$ nm. Wavelength dependent spectra were recorded with a 2.05 nm spectral resolution, collected using an Andor ICCD camera, and integrated over the first 500 ns after the pump laser pulse. The spectra are presented as $\Delta OD_{Xe\ lamp}$, which is simply referred to as ΔOD. Lifetime data was generated using a photomultiplier to collect time

resolved signals, with the bandwidth of these data being identical to the camera resolution (2.05 nm). The lifetime data is fit using the Origin 2017 software package, and each data set is fit using a monoexponential function, with no evidence of multiexponential components. Uncertainties in lifetimes are taken from the Least-Squares fitting algorithm, and are not indicative of the uncertainties in multiple fits or data sets.

Cyclic voltammetry

Electrochemical studies were carried out using a Parstat 2273 potentiostat in conjunction with a three-electrode cell. The auxiliary electrode was a platinum wire and the working electrode a platinum (1.0 mm diameter) disc. The reference was a silver wire separated from the test solution by a fine porosity frit and an agar bridge saturated with KCl. Solutions (10 ml CH_2Cl_2) were 1.0×10^{-3} mol dm^{-3} in the test compound and 0.1 mol dm^{-3} in $[NBu^n_4][PF_6]$ as the supporting electrolyte. Under these conditions, $E^{0\prime}$ for the one-electron oxidation of $[Fe(\eta\text{-}C_5H_5)_2]$, added to the test solutions as an internal calibrant, is +0.46 V. [36] Unless specified, all electrochemical values are at u = 200 mV s^{-1}.

Triplet-Triplet Annihilation Upconversion

Associated luminescence spectra were recorded on Shimadzu RF-5301PC spectrofluorometer. The fluorescence and phosphorescence lifetimes were measured on an OB920 fluorescence/phosphorescence lifetime instrument (Edinburgh, U.K.) with an EPL picosecond pulsed diode laser (510 nm $\pm$ 10 nm, pulse width: 119.9 ps, maximum average power: 5 mW; All compounds in flash photolysis experiments were deaerated with N_2 for *ca.* 10 min and the gas was maintained during the measurement.

Continuous laser (510 nm) was used for upconversion and the power of the laser beam was 5.2 mW. The diameter of the spot of the 510 nm laser was ca. 3 mm. The mixed solution (with different triplet sensitizers and acceptor) was deaerated for 10 min before experiment, and the gas flow was kept during the measurement. The upconverted fluorescence was recorded with a RF 5301PC spectrofluorometer. In order to repress the laser scattering, a small black box was put behind the fluorescent cuvette as beam dump to trap the laser.

The upconversion quantum yields (Φ_{UC}) of all the complexes in toluene were using the fluorescence quantum yield of diiodoBodipy (Φ_F = 2.7% in acetonitrile) as the standard to be determined. The upconversion quantum yield was using the following equation (Eq. 2) to calculate, where Φ, *A*, *I* and η represent the quantum yield, absorbance, integrated photoluminescence intensity and the refractive index, respectively. Symbols with 'std' and 'sam' are the corresponding parameters for the standard used in the measurement of quantum yield and samples to be measured.

$$\Phi_{UC} = 2\Phi_{std}\left(\frac{1-10^{-A_{std}}}{1-10^{-A_{sam}}}\right)\left(\frac{I_{sam}}{I_{std}}\right)\left(\frac{\eta_{sam}}{\eta_{std}}\right)^2$$

(Eq. 2)

Synthesis of 2-methyl-3-phenylquinoxaline, L1

1-phenyl-1,2-propanedione (2.0 mL, 15 mmol) and 1,2-diaminobenzene (1.60 g, 15 mmol) were dissolved in ethanol (30 mL) with acetic acid (1 mL). The reaction mixture was heated at reflux for 24 hours under a nitrogen atmosphere. The mixture was cooled to room temperature and the solvent removed *in vacuo*. The crude product was taken up in dichloromethane (20 mL) and washed with hydrochloric acid (0.1 M, 2 × 20 mL). The organic phase was dried over $MgSO_4$ and dried *in vacuo* to yield a low melting-point, yellow solid (3.26 g, 81 %). ^{1}H NMR (400 MHz; $CDCl_3$): δ_H 8.10 (1H, d, J_{HH} = 8.37 Hz), 8.05 (1H, d, J_{HH} = 8.37 Hz), 7.67-7.75 (3H, m), 7.65 (2H, d, J_{HH} = 7.15 Hz), 7.44-7.54 (3H, m), 2.77 (3H, s, Me), 2.51 (3H, s, Me) ppm; ^{13}C{^{1}H} NMR (75 MHz, $CDCl_3$): δ_C 155.7, 153.3, 142.0, 141.7, 139.8, 130.5, 130.0, 129.8, 129.7, 129.3, 129.1, 25.2 ppm. LR MS found *m/z* 220.1072, calcd *m/z* 220.1073 for $C_{15}H_{12}N_2$. UV-vis. ($CHCl_3$) λ_{max} (ε / dm^{3}mol^{-1}cm^{-1}): 325 (9400) nm. IR (solid) υ / cm^{-1} : 3061, 3032, 2961, 1952, 1813, 1686, 1611, 1578, 1557, 1508, 1495, 1483, 1443, 1431, 1395, 1375, 1341, 1248, 1217, 1188, 1132, 1117, 1074, 1030, 1005, 993, 974, 950, 921, 897, 868, 818, 797, 708, 679, 619, 608, 575, 559, 496, 467, 436, 409, 401.

Synthesis of L2

As L1 but with 1-phenyl-1,2-propanedione (246 mg, 1.7 mmol) and 1,2-diamino-4,5-dimethylbenzene (250 mg, 1.8 mmol). Product collected as a low melting-point, brown solid. (361 mg, 86 %). ^{1}H NMR (300 MHz, $CDCl_3$): δ_H 7.85 (s, 1H), 7.80 (s, 1H), 7.64 – 7.62 (m, 2H), 7.53 – 7.44 (m, 3H), 2.74 (s, 3H, Me), 2.50 (s, 3H, Me), 2.48 (s, 3H)

ppm; $^{13}C\{^1H\}$ NMR (101 MHz, $CDCl_3$): δ_C 153.92, 151.29, 140.27, 139.97, 139.62, 139.32, 128.97, 128.76, 128.49, 128.28, 127.33, 24.20, 20.44, 20.34 ppm. HRMS found *m/z* 249.1385, calcd *m/z* 249.1386 for $C_{17}H_{16}N_2$. UV-vis. ($CHCl_3$) λ_{max} (ε / $dm^3mol^{-1}cm^{-1}$): 339 (11200), 269 (11400), 262 (21800) nm. IR (solid) υ / cm^{-1} : 3060, 3030, 2961, 1654, 1483, 1445, 1398, 1373, 1337, 1252, 1217, 1204, 1157, 1123, 1076, 1024, 1003, 988, 920, 876, 870, 858, 785, 768, 739, 706, 696, 644, 629, 610, 559, 532, 494, 478, 440, 420, 403.

Synthesis of L3

As L1 but with 1-phenyl-1,2-propanedione (190 mg, 1.3 mmol) and 1,2-diamino-4,5-dichlorobenzene (250 mg, 1.4 mmol). Upon cooling to room temperature, a white precipitate formed and was collected by filtration. The precipitate was washed with methanol to yield the product as a white solid. (283 mg, 73 %). ^1H NMR (300 MHz, $CDCl_3$): δ_H 8.22 (s, 1H), 8.17 (s, 1H), 7.66 – 7.62 (m, 2H), 7.58 – 7.52 (m, 3H), 2.77 (s, 3H) ppm; $^{13}C\{^1H\}$ NMR (75 MHz, $CDCl_3$): δ_C 155.92, 154.01, 139.97, 139.77, 138.27, 133.69, 129.47, 129.12, 128.91, 128.69, 109.99, 24.54 ppm. HRMS found *m/z* 291.0268, calcd *m/z* 291.0264 for $C_{15}H_{10}Cl_2N_2$. UV-vis. ($CHCl_3$) λ_{max} (ε / $dm^3mol^{-1}cm^{-1}$): 342 (12800), 268 (30700) nm. IR (solid) υ / cm^{-1} : 3088, 1753, 1697, 1587, 1543, 1491, 1441, 1412, 1389, 1371, 1325, 1246, 1209, 1180, 1169, 1107, 1078, 1022, 1005, 993, 976, 955, 930, 897, 878, 845, 795, 768, 748, 706, 658, 635, 629, 613, 594, 550, 509, 490, 461, 428, 417.

Synthesis of L4

As for L1 but with 1-phenyl-1,2-propanedione (230 mg, 1.6 mmol) and 1,2-diamino-4,5-difluorobenzene (250 mg, 1.7 mmol). Upon cooling to room temperature, a white precipitate formed and was collected by filtration and washed with methanol. Product collected as a white solid. (225 mg, 55 %). ^1H NMR (300 MHz, $CDCl_3$): δ_H 7.87 – 7.77 (m, 2H), 7.65 – 7.62 (m, 2H), 7.56 – 7.49 (m, 3H), 2.76 (s, 3H) ppm; $^{13}C\{^1H\}$ NMR (101 MHz, $CDCl_3$): δ_C 138.44, 129.29, 128.88, 128.66, 114.78, 114.03, 24.29 ppm; $^{19}F\{^1H\}$ NMR (376 MHz, $CDCl_3$): δ_F -130.38 (d, $^3J_{FF}$ = 21.2 Hz), -131.17 (d, $^3J_{FF}$ = 21.2 Hz) ppm. HRMS found *m/z* 257.0888, calcd *m/z* 257.0885. UV-vis. ($CHCl_3$) λ_{max} (ε / $dm^3mol^{-1}cm^{-1}$): 326 (13000) nm. IR (solid) υ / cm^{-1} : 3030, 1630, 1572, 1553, 1497,

1450, 1373, 1356, 1339, 1256, 1227, 1200, 1142, 1078, 1015, 1005, 988, 928, 897, 874, 866, 791, 772, 752, 712, 706, 667, 619, 611, 584, 544, 484, 447, 419, 405.

Synthesis of L5

Benzil (357 mg, 1.7 mmol) and 1,2-diamino-4,5-dimethylbenzene (250 mg, 1.8 mmol) were dissolved in ethanol (15 mL) and acetic acid (1 mL). The reaction mixture was heated at reflux under a nitrogen atmosphere for 24 hours. The mixture was then cooled to room temperature and a white precipitate was collected by filtration and washed with methanol. (413 mg, 78 %). ^{1}H NMR (300 MHz, $CDCl_3$): δ_H 7.92 (s, 2H), 7.51 – 7.48 (m, 4H), 7.35 – 7.31 (m, 6H), 2.49 (s, 6H, Me) ppm; $^{13}C\{^{1}H\}$ NMR (75 MHz, $CDCl_3$): δ_C 152.50, 140.55, 140.21, 139.37, 129.84, 128.53, 128.21, 109.99, 20.50 ppm. HRMS found *m/z* 311.1542, calcd *m/z* 311.1543 for $C_{22}H_{18}N_2$. UV-vis. ($CHCl_3$) λ_{max} (ε / $dm^3mol^{-1}cm^{-1}$): 356 (13900), 281 (24600), 269 (31800), 254 (44900) nm. IR (solid) υ / cm^{-1} : 2974, 1749, 1549, 1531, 1493, 1474, 1460, 1445, 1416, 1400, 1375, 1346, 1335, 1263, 1211, 1179, 1153, 1074, 1059, 1022, 1003, 966, 932, 870, 849, 814, 783, 773, 762, 741, 725, 691, 633, 608, 598, 556, 530, 519, 492, 476, 436, 413.

Synthesis of L6

As L5 but with benzil (273 mg, 1.3 mmol) and 1,2-diamino-4,5-dichlorobenzene (250 mg, 1.4 mmol). Product collected as a white solid. (367 mg, 80 %). ^{1}H NMR (300 MHz, $CDCl_3$): δ_H 8.29 (s, 2H), 7.52 – 7.49 (m, 4H), 7.37 – 7.35 (m, 6H) ppm; $^{13}C\{^{1}H\}$ NMR (101 MHz, $CDCl_3$): δ_C 154.49, 139.95, 138.39, 134.43, 129.80, 129.29, 128.37 ppm. HRMS found *m/z* 351.0450, calcd *m/z* 351.0450 for $C_{20}H_{12}Cl_2N_2$. UV-vis. ($CHCl_3$) λ_{max} (ε / $dm^3mol^{-1}cm^{-1}$): 362 (19400), 254 (61300) nm. IR (solid) υ / cm^{-1} : 3067, 3024, 2980, 1589, 1535, 1491, 1452, 1439, 1393, 1337, 1254, 1190, 1109, 1074, 1061, 1020, 999, 964, 920, 883, 874, 831, 814, 766, 733, 719, 692, 640, 621, 606, 598, 546, 511, 488, 480, 444, 426, 419, 409.

Synthesis of L7

As L5, but with benzil (336 mg, 1.6 mmol) and 1,2-diamino-4,5-difluorobenzene (250 mg, 1.7 mmol). Product collected as an orange solid. (296 mg, 58 %). ^{1}H NMR (300 MHz, $CDCl_3$): δ_H 7.91 (app. td, *J* = 1.37, 9.35 Hz, 2H), 7.51 – 7.48 (m, 4H), 7.41 – 7.31

(m, 6H) ppm; $^{13}C\{^1H\}$ NMR (75 MHz, $CDCl_3$): δ_C 154.31, 154.07, 153.69, 150.89, 150.66, 138.51, 138.48, 129.77, 129.13, 128.37, 114.72 ppm; $^{19}F\{^1H\}$ NMR (376 MHz, $CDCl_3$): δ_F -129.86 ppm. HRMS found *m/z* 319.1044, calcd *m/z* 319.1041 for $C_{20}H_{12}F_2N_2$. UV-vis. ($CHCl_3$) λ_{max} (ε / $dm^3mol^{-1}cm^{-1}$): 343 (14900), 261 (16800) nm. IR (solid) υ / cm^{-1} : 3051, 1597, 1568, 1541, 1456, 1435, 1352, 1342, 1246, 1217, 1194, 1175, 1152, 1142, 1082, 1072, 1055, 1022, 1001, 972, 939, 918, 872, 818, 785, 772, 760, 752, 719, 700, 677, 623, 610, 573, 542, 521, 498, 438, 424, 419.

Complex Synthesis

$IrCl_3.xH_2O$ (1 eq.) and ligand, L (2 eq.) were dissolved in 2-ethoxyethanol (10 mL) and the reaction mixture heated at reflux for 48 hours. The reaction was then cooled to room temperature and water (30 mL) was added to form a dark brown precipitate. The solid was collected by filtration and assumed to yield $[Ir(L)_2\mu\text{-}Cl]_2$ and used without further purification.

Synthesis of $[Ir(L1)_2(bpy)]PF_6$

$[Ir(L1)_2\mu\text{-}Cl]_2$ (100 mg, 0.075 mmol) and 2,2′-bipyridyl (0.025 g, 0.16 mmol) were dissolved in 2-ethoxyethanol (10 mL) and heated at reflux for 24 hours under a nitrogen atmosphere. The reaction mixture was then cooled to room temperature and a saturated solution of aqueous ammonium hexafluorophosphate was added. Upon formation of a red precipitate, the mixture was filtered and the precipitate washed with water and diethyl ether to yield the product as a red solid. (0.08g, 68 %). ^1H NMR (300MHz, $CDCl_3$): δ_H 8.39 (2H, d, J_{HH} = 8.31 Hz), 8.24 (2H, d, J_{HH} = 8.31 Hz), 8.17 (2H, d, J_{HH} = 5.32 Hz), 8.01 (2H, app.t, J_{HH} = 7.86 Hz), 7.90 (2H, d, J_{HH} = 8.31 Hz), 7.45-7.57 (4H, m), 7.16-7.24 (2H, m), 7.00 (2H, app.t, J_{HH} = 7.69 Hz), 6.86 (2H, app. t, J_{HH} = 7.69 Hz), 6.61 (2H, d, J_{HH} = 7.60 Hz), 3.36 (6H, s, Me) ppm; $^{13}C\{^1H\}$ NMR (400MHz, $CDCl_3$): δ_C 163.7, 155.1, 152.6, 152.0, 146.6, 144.0, 140.4, 140.0, 139.7, 135.1, 130.9, 130.5, 130.4, 130.1, 129.2, 127.6, 124.8, 123.6, 123.2, 27.5 ppm. HRMS found *m/z* 787.2148, calcd *m/z* 787.2158 for $C_{40}H_{30}IrN_6$. UV-vis. ($CHCl_3$): λ_{max}/nm (ε / $dm^3mol^{-1}cm^{-1}$): 477 (2500), 372 (13200), 253 (27900) nm. IR (solid) υ / cm^{-1} : 1605, 1578, 1530, 1449, 1427, 1387, 1348, 1261, 1215, 1196, 1165, 1130, 1016, 1001, 897, 837, 770, 750, 731, 704, 660, 627, 592, 557, 459, 420, 415, 405.

Synthesis of $[Ir(L2)_2(bpy)]PF_6$

Product collected as a red solid (133 mg, 94 %). ^{1}H NMR: (400 MHz, Acetone-d_6): δ_H 8.57 – 8.54 (2 H, m), 8.49 (2 H, dd, J_{HH} = 8.3, 1.2 Hz), 8.41 (2 H, app. dt, J_{HH} = 8.2, 1.0Hz), 8.16 (2 H, ddd, J_{HH} = 8.3, 7.6, 1.6 Hz), 7.86 – 7.81 (2 H, m), 7.66 (2 H, s), 7.24 (2 H, ddd, J_{HH} = 8.3, 7.1, 1.3 Hz), 7.17 (2 H, s), 6.86 – 6.79 (2 H, m), 6.70 (2 H, dd, J_{HH} = 7.7, 1.3 Hz), 3.34 (6 H, s, Me), 2.30 (6 H, s, Me), 1.81 (6 H, s, Me) ppm; ^{13}C {^{1}H} (101 MHz, Acetone-d_6): δ_C 164.56, 156.84, 154.00, 153.38, 149.62, 146.39, 142.69, 142.14, 141.53, 140.70, 140.05, 136.48, 132.09, 131.63, 130.00, 129.66, 125.61, 125.24, 124.33, 28.18, 20.36, 20.11 ppm. HRMS found *m/z* 843.2783 calcd *m/z* 843.2784 for $C_{44}H_{38}IrN_6$. UV-vis ($CHCl_3$) λ_{max} (ε / $dm^3mol^{-1}cm^{-1}$): 474 (4800), 391 (22100), 376 (23900), 309 (19300), 390 (32300), 268 (47200) nm. IR (solid) υ / cm^{-1} : 1601, 1582, 1560, 1526, 1483, 1445, 1396, 1375, 1342, 1323, 1267, 1219, 1171, 1134, 1063, 993, 835, 795, 768, 737, 702, 660, 627, 556, 474, 434, 420, 403.

Synthesis of $[Ir(L3)_2(bpy)]PF_6$

As $[Ir(L1)_2(bpy)]PF_6$ but with $[Ir(L3)_2Cl]_2$ (100 mg, 0.06 mmol) and 2,2′-bipyridine (20 mg, 0.1 mmol). Product collected as a red solid (61 mg, 46 %). ^{1}H NMR (400 MHz, Acetone-d_6): δ_H 8.60 (2 H, d, J_{HH} = 8.4), 8.51 (3 H, dd, J_{HH} = 5.6, 3.6), 8.48 (1 H, s), 8.26 – 8.18 (2 H, m), 8.13 (2 H, d, J_{HH} = 1.2), 7.92 – 7.83 (2 H, m), 7.59 (2 H, s), 7.31 (2 H, dd, J_{HH} = 8.3, 6.7), 6.97 – 6.89 (2 H, m), 6.86 (1 H, s), 6.84 (1 H, s), 3.41 (6 H, s) ppm. ^{13}C {^{1}H} NMR (126 MHz, DMSO): δ_C 165.56, 155.14, 154.80, 153.75, 147.29, 143.91, 140.79, 138.80, 138.42, 135.28, 133.16, 132.60, 132.14, 131.53, 129.82, 129.31, 125.05, 124.96, 123.41, 27.34 ppm. HRMS found *m/z* 925.0548, calculated *m/z* 925.0558 for $C_{40}H_{26}Cl_4IrN_6$. UV-vis. ($CHCl_3$) λ_{max} (ε / $dm^3mol^{-1}cm^{-1}$): 500 (4500), 383 (23700), 298 (28900), 266 (48200) nm. IR (solid) υ / cm^{-1} : 1603, 1576, 1528, 1464, 1447, 1381, 1315, 1265, 1188, 1165, 1132, 1113, 1061, 1026, 1009, 962, 895, 870, 843, 824, 772, 739, 729, 673, 664, 646, 637, 608, 556, 467, 428, 419, 403.

Synthesis of $[Ir(L4)_2(bpy)]PF_6$

Product collected as a red solid (133 mg, 97 %). ^{1}H NMR (400 MHz, Acetone-d_6): δ_H 8.58 (2 H, dd, J_{HH} = 8.3, 1.2), 8.54 (2 H, ddd, J_{HH} = 5.5, 1.6, 0.8), 8.47 (2 H, dt, J_{HH} = 8.2, 1.0), 8.25 – 8.18 (2 H, m), 7.92 – 7.81 (4 H, m), 7.34 – 7.20 (4 H, m), 6.95 – 6.88

(2 H, m), 6.84 – 6.79 (2 H, m) ppm. ^{13}C {^{1}H} NMR (101 MHz, Acetone-d_6): δ_C 155.55, 152.77, 147.77, 144.41, 140.52, 135.29, 131.51, 131.13, 128.91, 124.79, 123.34 ppm. ^{19}F NMR (376 MHz, Acetone-d_6): δ_F -72.63 (d, J = 711.7 Hz), -131.73 (d, J = 21.9 Hz), -133.10 (d, J = 21.9 Hz) ppm. HRMS found *m/z* 859.1780, calculated *m/z* 859.1781 for $C_{40}H_{26}F_4IrN_6$. UV-vis. ($CHCl_3$) λ_{max} (ε / $dm^3mol^{-1}cm^{-1}$): 480 (2400), 375 (13200), 311(11800), 288 (15400), 262 (25800) nm. IR (solid) υ / cm^{-1} : 1065, 1578, 1533, 1501, 1447, 1341, 1331, 1252, 1233, 1196, 1128, 1063, 1036, 997, 878, 841, 795, 772, 741, 731, 689, 660, 638, 586, 557, 476, 451, 428, 422, 407.

Synthesis of $[Ir(L5)_2(bpy)]PF_6$

As $[Ir(L1)_2(bpy)]PF_6$ but with $[Ir(L5)_2Cl]_2$ (150 mg, 0.09 mmol) and 2,2′-bipyridine (29 mg, 0.2 mmol). Product collected as a red solid (124 mg, 63%). ^{1}H NMR (400 MHz, Acetone-d_6): δ_H 9.10 (2 H, dt, J_{HH} = 5.1, 2.2), 8.61 – 8.52 (2 H, m), 8.34 – 8.25 (2 H, m), 8.24 – 8.15 (2 H, m), 7.96 (4 H, dt, J_{HH} = 6.7, 2.7), 7.78 (2 H, s), 7.74 – 7.65 (6 H, m), 7.34 (2 H, s), 7.18 (2 H, ddd, J_{HH} = 8.2, 2.9, 1.5), 6.78 – 6.72 (2 H, m), 6.69 – 6.63 (2 H,m), 6.61 – 6.54 (2 H, m), 2.35 (6 H, s), 1.94 (6 H, s) ppm. ^{13}C {^{1}H} NMR (101 MHz, Acetone-d_6): δ_C 162.58, 156.09, 153.60, 152.81, 149.26, 144.93, 142.80, 141.53, 140.81, 140.42, 139.91, 139.43, 135.23, 131.40, 130.46, 130.06, 129.58, 129.44, 129.21, 124.84, 123.98, 122.37, 19.43, 18.99 ppm. HRMS found *m/z* 967.3086, calcd *m/z* 967.3099 for $C_{54}H_{42}IrN_6$. UV-vis. ($CHCl_3$) λ_{max} (ε / $dm^3mol^{-1}cm^{-1}$): 479 (6500), 400 (29300), 362 (24800), 297 (49000), 269 (71300) nm. IR (solid) υ / cm^{-1}: 1603, 1580, 1479, 1447, 1348, 1321, 1234, 1207, 1159, 1134, 1074, 1024, 1001, 974, 833, 810, 775, 748, 737, 729, 700, 658, 640, 608, 577, 557, 542, 446, 432, 415.

Synthesis of $[Ir(L6)_2(bpy)]PF_6$

As $[Ir(L1)_2(bpy)]PF_6$, but with $[Ir(L6)_2Cl]_2$ (100 mg, 0.05 mmol) and 2,2′-bipyridine (19 mg, 0.1 mmol). Product collected as a red solid (48 mg, 37 %). ^{1}H NMR (300 MHz, Acetone-d_6): δ_H 8.98 (2 H, ddd, J_{HH} = 5.5, 1.7, 0.7), 8.60 (2 H, dt, J_{HH} = 8.2, 1.0), 8.30 (2 H, td, J_{HH} = 7.9, 1.6), 8.23 – 8.15 (4 H, m), 7.99 – 7.90 (4 H, m), 7.69 (8 H, q, J_{HH} = 2.2, 1.8), 7.25 – 7.15 (2 H, m), 6.81 – 6.62 (6 H, m) ppm. ^{13}C {^{1}H} NMR (101 MHz, Acetone-d_6): δ_C 166.36, 157.25, 156.93, 155.10, 149.90, 145.27, 142.19, 141.00, 140.74, 140.57, 136.52, 136.16, 133.44, 132.75, 131.91, 131.67, 130.77, 130.55, 126.65, 126.43, 123.84 ppm. HRMS found *m/z* 1049.0839, calculated *m/z* 1049.0872

for $C_{50}H_{30}Cl_4IrN_6$. UV-vis. λ_{max} / nm ($CHCl_3$) 501(7300), 404 (35300), 299 (54600), 268 (87500) nm. IR (solid) υ / cm^{-1}: 1603, 1576, 1524, 1493, 1445, 1433, 1406, 1383, 1342, 1317, 1258, 1186, 1165, 1132, 1115, 1072, 1045, 1026, 1001, 961, 880, 839, 826, 766, 734, 698, 673, 648, 635, 606, 577, 557, 532, 517, 486, 474, 451, 434, 419.

Synthesis of $[Ir(L7)_2(bpy)]PF_6$

As $[Ir(L1)_2(bpy)]PF_6$ but with $[Ir(L7)_2Cl]_2$ (100 mg, 0.06 mmol) and 2,2'-bipyridine (19 mg, 0.1 mmol). Product collected as a red solid (108 mg, 83 %). ^{1}H NMR (400 MHz, Acetone-d_6): δ_H 9.10 – 9.06 (2 H, m), 8.63 (2 H, d, J_{HH} = 8.2), 8.35 (2 H, tt, J_{HH} = 8.0, 1.4), 8.22 (2 H, m), 8.01 (6 H, tt, J_{HH} = 8.5, 4.4), 7.79 – 7.68 (6 H, m), 7.55 (1 H, dt, J_{HH} = 8.2, 1.5), 7.46 – 7.37 (2 H, m), 7.28 – 7.20 (2 H, m), 6.87 – 6.79 (2 H, m), 6.77 – 6.72 (2 H, m), 6.69 (2 H, dt, J_{HH} = 7.8, 1.3) ppm. ^{13}C {^{1}H} NMR (101 MHz, Acetone-d_6): δ_C 157.50, 150.05, 142.41, 140.79, 136.71, 133.25, 132.55, 131.76, 130.75, 126.56, 124.00, 117.87 ppm. ^{19}F{^{1}H} NMR (376 MHz, Acetone-d_6): δ_F -72.64 (d, J = 699.9 Hz), -130.30 (d, J = 21.7 Hz), -132.66 (d, J = 21.7 Hz) ppm. HRMS found *m/z* 983.2088, calculated *m/z* 983.2095 for $C_{50}H_{30}F_4IrN_6$. UV-vis. ($CHCl_3$) λ_{max} (ε / $dm^3mol^{-1}cm^{-1}$): 483 (4500), 396 (21600), 367 (20200), 297 (33100), 265 (48600) nm. IR (solid) υ / cm^{-1} : 1603, 1578, 1503, 1447, 1429, 1335, 1275, 1260, 1223, 1204, 1163, 1126, 1072, 1043, 1026, 980, 874, 835, 810, 758, 739, 700, 660, 640, 623, 615, 557, 536, 498.

Acknowledgements

Cardiff University (Knowledge Economy Skills Scholarship to KAP) and STG Aerospace are thanked for financial support. We thank the staff of the Engineering and Physical Sciences Research Council (EPSRC) Mass Spectrometry National Service (Swansea University) for providing MS data and the Engineering and Physical Sciences Research Council (EPSRC) UK National Crystallographic Service at the University of Southampton. JMB acknowledges Dr. James A. Platts for helpful discussions regarding the Gaussian calculations.

Keywords: Iridium complex • Spectroscopy • Upconversion • Phosphors • DFT

Notes and references

‡ CCDC1825271, 1825273 and 1825272 contains supplementary X-ray crystallographic data for **[Ir(L2)$_2$(bpy)]PF$_6$**, **[Ir(L5)$_2$(bpy)]PF$_6$** and **[Ir(L7)$_2$(bpy)]PF$_6$** respectively. This data can be obtained free of charge via http://www.ccdc.cam.ac.uk/structures/, or from the Cambridge Crystallographic Data Centre, Union Road, Cambridge, CB2 1EZ; fax(+44) 1223-336-033 or email: deposit@ccdc.cam.ac.uk.

Corresponding Authors:

Prof. Simon J. A. Pope:

E-mail: PopeSJ@cardiff.ac.uk

Dr Joseph M. Beames:

E-mail: BeamesJ@cardiff.ac.uk

Figures and Captions

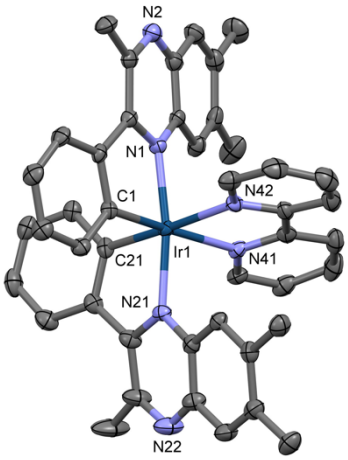

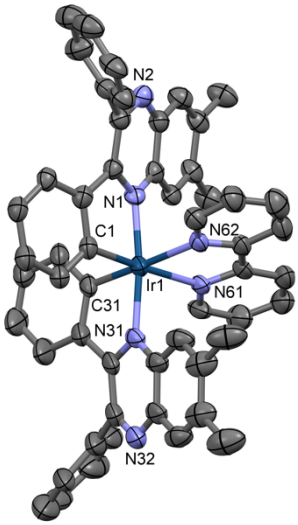

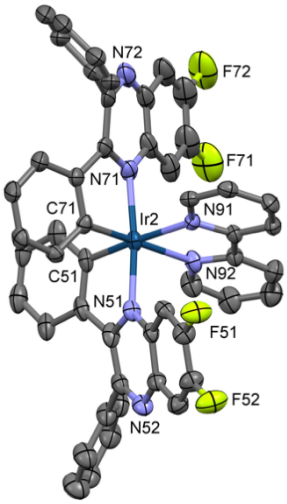

Figure 1. X-ray structures of the complexes **[Ir(L2)$_2$(bpy)]PF$_6$**, **[Ir(L5)$_2$(bpy)]PF$_6$** and **[Ir(L7)$_2$(bpy)]PF$_6$** (top to bottom). Anions and solvents of crystallisation are omitted.

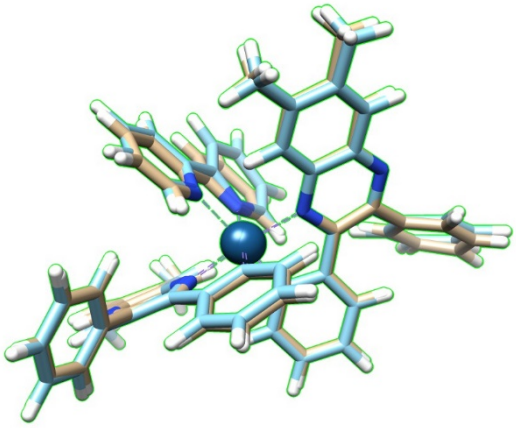

Figure 2. Overlay of the crystal structure (blue) and DF-DFT//B3LYP/6-31G*(SDD) optimised structures (brown) for **[Ir(L5)$_2$(bpy)]PF$_6$**. The structures exhibit an RMSD of 0.3 Å.

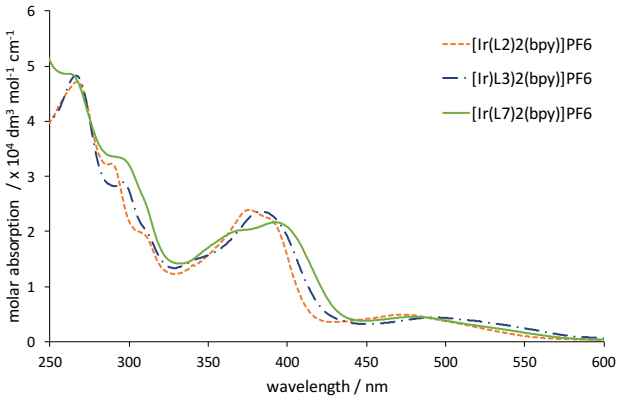

Figure 3. Absorption spectra of **[Ir(L2)$_2$(bpy)]PF$_6$**, **[Ir(L3)$_2$(bpy)]PF$_6$**, **[Ir(L7)$_2$(bpy)]PF$_6$** (in chloroform).

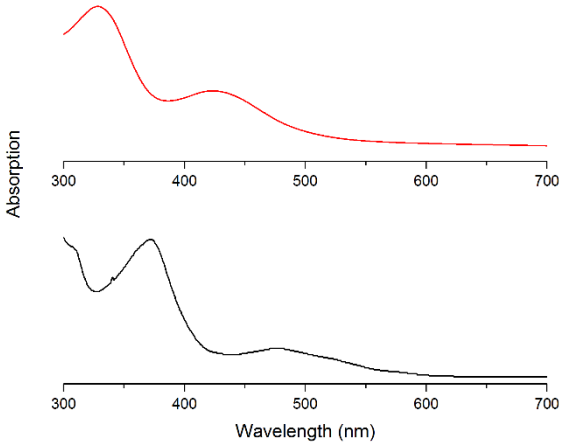

Figure 4. Comparison of the experimental absorption spectrum of **$[Ir(L1)_2(bpy)]PF_6$** (black) with the TDDFT//CAM-B3LYP/6-31G*(SDD) convoluted absorption spectrum (dashed red), computed the method described in the text. The red line is a summation of spin allowed and spin forbidden transition energies, where all spin forbidden transitions are assigned an identical oscillator strength, with the total summative transition strength chosen to best illustrate the spectrum.

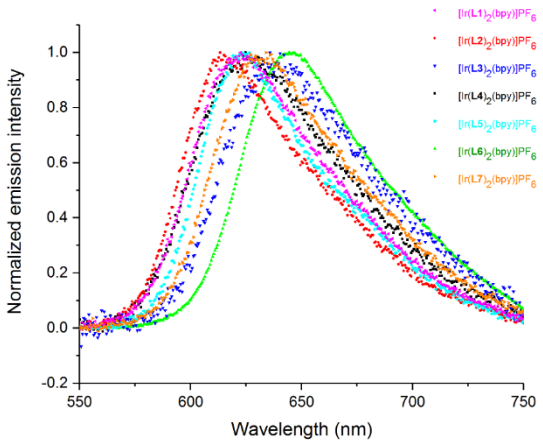

Figure 5. Normalized emission spectra of complexes (in chloroform, λ_{ex} = 355 nm).

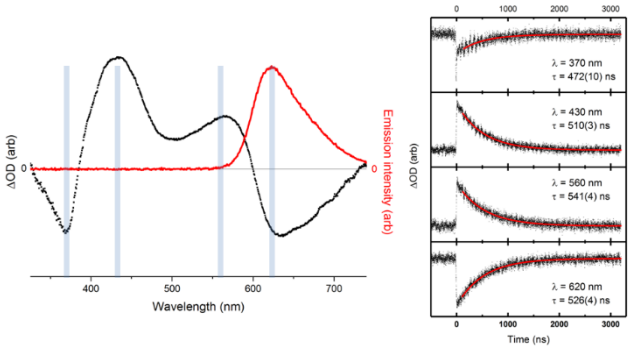

Figure 6. Left: transient absorption spectrum of **[Ir(L1)$_2$(bpy)]PF$_6$** shown in black, overlaid with the emission spectrum of the same complex shown in red. Right: transient absorption lifetime measurements made at selected wavelengths, highlighted as grey bars in the right hand figure. The red traces indicate monoexponential fits to these measurements, with corresponding lifetimes displayed in each panel. Recorded in chloroform, λ_{ex} = 355 nm.

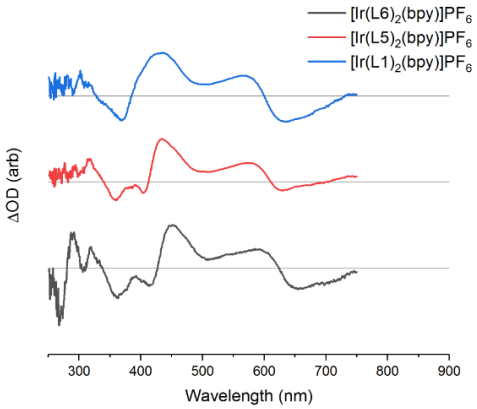

Figure 7. Transient absorption spectra of several sample complexes. The spectra show qualitatively similar features. Recorded in chloroform, λ_{ex} = 355 nm.

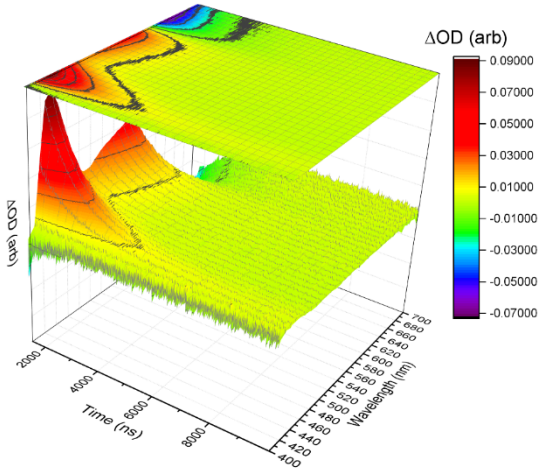

Figure 8. Sample time resolved transient absorption data for **[Ir(L6)$_2$(bpy)]PF$_6$** prior to spectral deconvolution. The data is shown from t = 1800 ns for clarity purposes only.

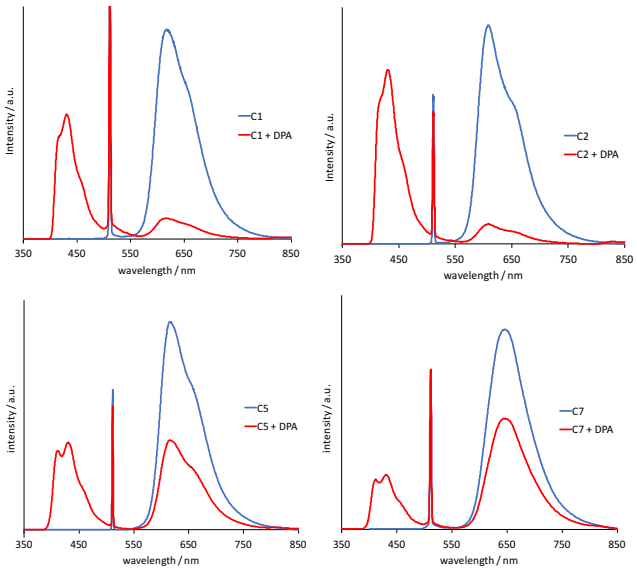

Figure 9. Clockwise from top left: the upconversion fluorescence spectra of **C1 [Ir(L1)$_2$(bpy)]PF$_6$**, **C2 [Ir(L2)$_2$(bpy)]PF$_6$**, **C7 [Ir(L7)$_2$(bpy)]PF$_6$**, and **C5 [Ir(L5)$_2$(bpy)]PF$_6$** as photosensitizer in toluene. **DPA** (9,10-diphenylanthracene) was the acceptor. Excitation was done with a continuous laser at 510 nm (noted as the incident peak on the spectra) and power density of 5.2 mW under deaerated atmosphere. *c* (sensitizer) = 1.0×10^{-5} M, *c* (**DPA**) were 1.6×10^{-3} M, 1.6×10^{-3} M, 2.6×10^{-4} M, 2.0×10^{-4} M, respectively, 20 °C.

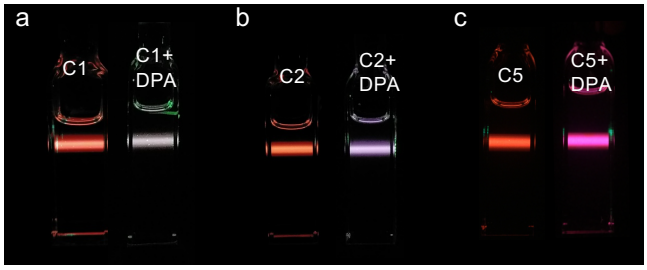

Figure 10. Photographs of the emission of selected triplet sensitizers **C1** **[Ir(L1)$_2$(bpy)]PF$_6$**, **C2** **[Ir(L2)$_2$(bpy)]PF$_6$** and **C5** **[Ir(L5)$_2$(bpy)]PF$_6$** alone and the upconversion with **DPA** in toluene. Excitation was done with a continuous laser of 510 nm and power density of 5.2 mW under deaerated atmosphere. *c* (sensitizers) = 1.0 × 10^{-5} M; *c* (**DPA**) were (a) 1.6 × 10^{-3} M, (b) 1.6 × 10^{-3} M, (c) 2.0 × 10^{-4} M, respectively, 20 °C.

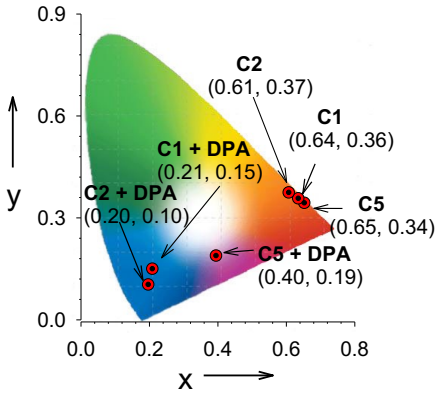

Figure 11. The CIE coordinate changes of triplet sensitizers **C1** **[Ir(L1)$_2$(bpy)]PF$_6$**, **C2** **[Ir(L2)$_2$(bpy)]PF$_6$** and **C5** **[Ir(L5)$_2$(bpy)]PF$_6$** before and after adding **DPA**. Excitation was done with a continuous laser of 510 nm and power density of 5.2 mW under deaerated atmosphere. Before: *c* (Sensitizers) = 1.0 × 10^{-5} M. After: **DPA** were added with 1.6 × 10^{-3} M for **C1**, 1.6 × 10^{-3} M for **C2**, 2.0 × 10^{-4} M for **C4** and 2.0 × 10^{-4} M for **C5**, respectively, 20 °C.

Schemes and captions

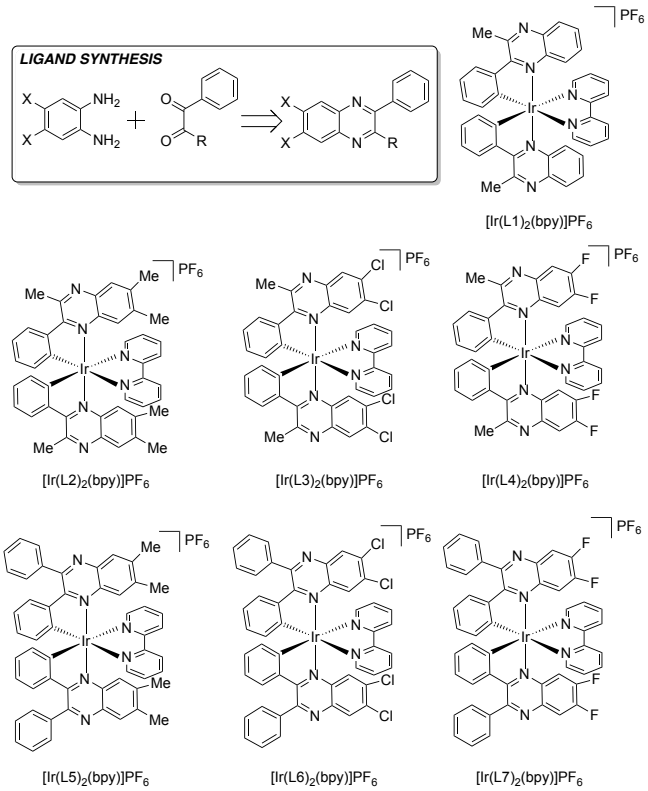

Scheme 1. Structures of the heteroleptic Ir(III) complexes synthesised in the study and the generalised route to the ligands (top and inset).

TOC text

A series of substituted 2-phenylquinoxaline ligands have been explored to finely tune the visible emission properties of a corresponding set of cationic, cyclometalated iridium(III) complexes.. The complexes were assessed as sensitizers in triplet-triplet annihilation upconversion experiments, demonstrating highly impressive upconversion quantum yields of up to 39 %.

References

[1] a) S. Ladouceur, E. Zysman-Colman, *Eur. J. Inorg. Chem*. **2013**, 2985; b) A. Ruggi, F.W.B. van Leeuwen, A.H. Velders, *Coord. Chem. Rev*. **2011**, *255*, 2542; c) K. K-W. Lo, M-W. Louie, K.Y. Zhang, *Coord. Chem. Rev*. **2010**, *254*, 2603; d) A. F. Henwood, E. Zysman-Colman, *Chem. Commun*. **2017**, *53*, 807.

[2] a) T.N. Singh-Rachford, F.N. Castellano, *Coord. Chem. Rev*. **2010**, *254*, 2560; b) S. Baluschev, T. Miteva, V. Yakutkin, G. Nelles, A. Yasuda, G. Wegner, *Phys. Rev. Lett*. **2006**, *97*, 143903;

[3] a) J. Peng, X. Jiang, X. Guo, D. Zhao, Y. Ma, *Chem. Commun*. **2014**, *50*, 7828; b) P. Duan, N. Yanai, N. Kimizuka, *Chem. Commun*. **2014**, *50*, 13111; c) J. Sun, F. Zhong, X Yi, J. Zhao, *Inorg. Chem*. **2013**, *52*, 6299; d) J. Ma, X. Cui, F. Wang, X. Wu, J. Zhao, K. Li, *J. Org. Chem*. **2014**, *79*, 10855; e) Y. Lu, N. McGoldrick, F. Murphy, B. Twamley, X. Cui, C. Delaney, G.M. O Maille, J. Wang, J. Zhao, S.M. Draper, *Chem. Eur. J*. **2016**, *22*, 11349; f) J. Sun, W. Wu, H. Guo, J. Zhao, *Eur. J. Inorg. Chem*. **2011**, 3165; g) J. Sun, W. Wu, J. Zhao, *Chem. Eur. J*. **2012**, *18*, 8100; g) C.E. McCusker, F.N. Castellano, *Inorg. Chem*. **2015**, *54*, 6035; h) P. Wang, Y.H. Lee, W. Kim, W. Yang, X. Cui, W. Ji, J. Zhao, D. Kim, *J. Phys. Chem. C* **2017**, *121*, 11117.

[4] For example: a) X. Yi, P. Yang, D. Huang, J. Zhao, *Dyes and Pigments* **2013**, *96*, 104; b) L. Ma, H. Guo, Q. Li, S. Guo, J. Zhao, *Dalton Trans*. **2012**, *41*, 10680; c) X. Yi, C. Zhang, S. Guo, J. Ma, J. Zhao, *Dalton Trans*. **2014**, *43*, 1672; d) X. Chu, M. Guan, L. Niu, Y. Zeng, Y. Li, Y. Zhang, Z. Zhu, B. Wang, *ACS Appl. Mater. Interfaces* **2014**, *6*, 19011.

[5] Y. Lu, J. Wang, N. McGoldrick, X. Cui, J. Zhao, C. Caverly, B. Twamley, G.M.O Maille, B. Irwin, R. Conway-Kenny, S.M. Draper, *Angew. Chem. Int. Ed*. **2016**, *55*, 14688.

[6] J. Zhao, W. Wu, J. Sun, S. Guo, *Chem. Soc. Rev*. **2013**, *42*, 5323

[7] R.A. Smith, E.C. Stokes, E.E. Langdon-Jones, J.A. Platts, B.M. Kariuki, A.J. Hallett, S.J.A. Pope, *Dalton Trans*. **2013**, *42*, 10347.

[8] E.E. Langdon-Jones, A.J. Hallett, J.D. Routledge, D.A. Crole, B.D. Ward, J.A. Platts, S.J.A. Pope, *Inorg. Chem*. **2013**, *52*, 448

[9] A.J. Hallett, N. White, W. Wu, X. Cui, P.N. Horton, S.J. Coles, J. Zhao, S.J.A. Pope, *Chem. Commun*. **2012**, *48*, 10838

[10] For example, a) J. Xue, L. Xin, J. Hou, L. Duan, R. Wang, Y. Wei, J. Qiao, *Chem. Mater*. **2017**, *29*, 4775; b) L. Wang, H. Yin, P. Cui, M. Hetu, C. Wang, S. Monro, R.D. Schaller, C.G. Cameron, B. Liu, S. Kilina, S.A. McFarland, W. Sun, *Dalton Trans*. **2017**, *46*, 8091.

[11] M. Nonoyama, *Bull. Chem. Soc. Jpn*. **1974**, *47*, 767

[12] a) A.B. Tamayo, B.D. Alleyne, P.I. Djurovich, S. Lamansky, I. Tsyba, N.M. Ho, R. Bau, M.E. Thompson, *J. Am. Chem. Soc*. **2003**, *125*, 7377; b) S. Lamansky, P. Djurovich, D. Murphy, F. Abdel-Razzaq, R. Kwong, I. Tsyba, M. Bortz, B. Mui, R. Bau, M.E. Thompson, *Inorg. Chem*. **2001**, *40*, 1704; c) M.C. Colombo, T.C. Brunold, T. Riedener, H.U. Gudel, M. Fortsch, H-B. Burgi, *Inorg. Chem*. **1994**, *33*, 545

[13] J.M. Fernandez-Hernandez, C-H. Yang, J.I. Beltran, V. Lemaur, F. Polo, R. Frohlich, J. Cornil, L. De Cola, *J. Am. Chem. Soc*. **2011**, *133*, 10543.

[14] a) S. Ammerman, C. Hrib, P.G. Jones, W-W. du Mont, W. Kowalsky, H-H. Johannes, *Org. Lett*. **2012**, *14*, 5090; b) E. Matteucci, A. Baschieri, A. Mazzanti, L. Sambri, J. Avila, A. Pertegas, H.J. Bolink, F. Monti, E. Leoni, N. Armaroli, *Inorg. Chem*. **2017**, *56*, 10584.

[15] N. Castillo, C.F. Matta, R.J. Boyd, *J. Chem. Inf. Model*. **2005**, *45*, 354

[16] a) M. Polson, S. Fracasso, V. Bertolasi, M. Ravaglia, F. Scandola, *Inorg. Chem*. **2004**, *43*, 1950; b) M. Albrect, *Chem. Rev*. **2010**, *110*, 576; c) B.J. Coe, S.J. Glenwright, *Coord. Chem. Rev*. **2000**, *203*, 5

[17] N. M. O'Boyle, A. L. Tenderholt and K. M. Langner. *J. Comp. Chem*. **2008**, *29*, 839

[18] Gaussian 09, Revision C.01, M. J. Frisch, G. W. Trucks, H. B. Schlegel, G. E. Scuseria, M. A. Robb, J. R. Cheeseman, G. Scalmani, V. Barone, G. A. Petersson, H. Nakatsuji, X. Li, M. Caricato, A. Marenich, J. Bloino, B. G. Janesko, R. Gomperts, B. Mennucci, H. P. Hratchian, J. V. Ortiz, A. F. Izmaylov, J. L. Sonnenberg, D. Williams-Young, F. Ding, F. Lipparini, F. Egidi, J.

Goings, B. Peng, A. Petrone, T. Henderson, D. Ranasinghe, V. G. Zakrzewski, J. Gao, N. Rega, G. Zheng, W. Liang, M. Hada, M. Ehara, K. Toyota, R. Fukuda, J. Hasegawa, M. Ishida, T. Nakajima, Y. Honda, O. Kitao, H. Nakai, T. Vreven, K. Throssell, J. A. Montgomery, Jr., J. E. Peralta, F. Ogliaro, M. Bearpark, J. J. Heyd, E. Brothers, K. N. Kudin, V. N. Staroverov, T. Keith, R. Kobayashi, J. Normand, K. Raghavachari, A. Rendell, J. C. Burant, S. S. Iyengar, J. Tomasi, M. Cossi, J. M. Millam, M. Klene, C. Adamo, R. Cammi, J. W. Ochterski, R. L. Martin, K. Morokuma, O. Farkas, J. B. Foresman, and D. J. Fox, Gaussian, Inc., Wallingford CT, 2016.

[19] M. Barbatti, M. Ruckenbauer, F. Plasser, J. Pittner, G. Granucci, M. Persico, H. Lischka, *Comp. Mol. Sci*. **2014**, *4*, 26.

[20] M. Barbatti, G. Granucci, M. Ruckenbauer, F. Plasser, R. Crespo-Otero, J. Pittner, M. Persico,
H. Lischka, NEWTON-X: A package for Newtonian dynamics close to the crossing seam. Version 2, 2016, www.newtonx.org.

[21] A. Juris, V. Balzani, F. Barigelletti, S. Campagna, P. Belser, A. von Zelewsky, *Coord. Chem. Rev*. **1988**, *84*, 85

[22] L.M. Groves, C. Schotten, J. Beames, J.A. Platts, S.J. Coles, P.N. Horton, D.L. Browne, S.J.A. Pope, *Chem. Eur. J*. **201**7, *23*, 9407.

[23] D. Dzembo, K. Borjesson, V. Gray, K. Moth-Poulsen, B. Albinsson, *J. Phys. Chem. C* **2016**, *120*, 23397;

[24] S. J. Coles, P. A. Gale, *Chem. Sci*. **2012**, *3*, 683.

[25] O. V. Dolomanov, L. J. Bourhis, R. J. Gildea, J. A. K. Howard, H. Puschmann, *J. Appl. Crystallogr*. **2009**, *42*, 339.

[26] G. M. Sheldrick, *Acta Crystallogr. Sect. A* **2015**, *71*, 3.

[27] G. M. Sheldrick, *Acta Crystallogr. Sect. C* **2015**, *27*, 3.

[28] E.F. Pettersen, T.D. Goddard, C.C. Huang, G.S. Couch, D.M. Greenblatt, E.C. Meng, T.E. Ferrin, *J. Comput. Chem*. **2004**, *25*, 1605. http://www.cgl.ucsf.edu/chimera